IOP Publishing Journal of Optics
J. Opt. **26** (2024) 035604 (8pp) https://doi.org/10.1088/2040-8986/ad237c

Fourier-transform-only method for random phase shifting interferometry

Alperen Saltik[1], **Sueda Saylan**[1] and **Onur Tokel**[1,2,*]

[1] Department of Physics, Bilkent University, Ankara 06800, Turkey
[2] UNAM—National Nanotechnology Research Center and Institute of Materials Science and Nanotechnology, Bilkent University, Ankara 06800, Turkey

E-mail: otokel@bilkent.edu.tr

Received 4 August 2023, revised 22 December 2023
Accepted for publication 29 January 2024
Published 8 February 2024

Abstract

An accurate and computationally simple phase shifting interferometry (PSI) method is developed to reconstruct phase maps without *a priori* knowledge of the phase shift. Previous methods developed for random PSI either do not address general sources of error or require complex iterative processes and increased computational time. Here we demonstrate a novel method that is able to extract the phase using only Fourier transform (FT). With spatial FT analysis, randomly phase-shifted data is reordered to allow performing temporal FT on the intensity, which is a function of the phase shift. Since the entire process, including order analysis and phase calculation, is based only on Fourier analysis, it is rapid, easy to implement, and addresses general sources of error. The method exhibits high performance in experiments containing random phase shifts. Moreover, simulations incorporating common experimental error sources such as random intensity noise, intensity harmonics, and phase shift errors demonstrate that the proposed method performs as good as or better than the state-of-the-art phase reconstruction techniques in terms of accuracy and time.

Supplementary material for this article is available online

Keywords: phase microscopy, phase shifting interferometry, Fourier analysis

1. Introduction

Phase-shifting interferometry (PSI) is a powerful tool for nondestructive characterization of samples with low absorption characteristics [1]. In the most general case, PSI requires multiple phase-shifted images, since both amplitude and phase information needs to be decoupled from the intensity images. Conventional analytical solutions for PSI require constant phase shift increments between three or more interferograms [2–4]. However, in practice, a variety of factors come into play, including phase-shift errors, nonuniform phase-shift distribution, intensity harmonics due to detector nonlinearities, and random intensity noise [5, 6]. Thus, the necessity for precise, constant, and known phase shifts limits the application of conventional methods [7]. Although a family of intensity averaging algorithms have been proposed to reduce phase shifting errors [5, 8], these algorithms require the phase shifts to be equal. For nonequal phase shifts, methods based on least-square (L-S) fitting have been proposed [9], but they also suffer from intensity harmonics [10].

A number of algorithms have been proposed to address arbitrary and unknown phase shifting, including advanced iterative algorithm (AIA), the algorithm based on principle component analysis (PCA), the algorithm for self-calibrating generalized PSI and the algorithm based on VU factorization [11–14]. However, these algorithms do not consider nonuniform phase shifts, where the phase shift has spatial dependency, or intensity harmonics. Thus a method that works with general sources of error is required. Recently, such a method based on general iterative algorithm (GIA) has been proposed [15]. However, it is also based on computationally complex iterative processes, and requires long computational time. Contrarily,

* Author to whom any correspondence should be addressed.

Fourier analysis is a widely-known, general, and rapid tool for the analysis of harmonic patterns incorporating noise. Yet, the previously introduced Fourier-transform (FT) based techniques require evenly-spaced phase shifting [16, 17]. In this work, we propose a novel algorithm that is based only on Fourier-transform and is able to extract the phase from unknown, randomly phase-shifted fringe patterns, accounting for the most general sources of error.

Constant phase shifts between interferograms generate a periodic intensity waveform for a given pixel [7]. However, phase shift errors result in deviations from an ideal sinusoidal waveform. Therefore, approaches to extract the phase from nonsinusoidal intensity waveforms are needed. The present work reports a novel method that generates a sinusoidal intensity waveform from randomly phase-shifted interferograms by utilizing a spatial FT approach. This further allows obtaining the unknown phase via temporal FT, which is otherwise not possible for randomly phase-shifted patterns. This may also represent an important solution for other optical metrology applications that utilize Fourier analysis. Phase retrieval is the centerpiece of numerous measurement techniques, including noninvasive measurements of refractive index, and subsequent determinations of temperature and density, as well as deformation and displacement measurements. Further, applications such as digital holography, interference microscopy, speckle interferometry, optical coherence tomography, and FT spectroscopy all underscore the method's potential breadth of impact [18–22].

The proposed algorithm relaxes the restrictions imposed on the phase steps between the interferograms and corrects for well-known phase imaging errors including random intensity noise, intensity harmonics, and phase shift errors. As verified by simulations and experiments, it demonstrates robustness to these error sources and produces accurate results with both low- and high-resolution mechanical stepping equipment. Another major advantage of the proposed approach is that it purely relies on the well-known Fourier theory. Further, the intensity is not analyzed pixel by pixel, which renders our method computationally cost-effective compared to methods that use intensity minimum-maximum comparison [23].

2. Methodology

The setup used in our experiments for phase imaging is shown in figure 1. Phase shifts are achieved by translating a mirror in the sample arm with a piezoelectric stage (NF15AP25/M, Thorlabs, theoretical resolution of ~ 0.76 nm), which is controlled by a piezo controller (Thorlabs KPZ101) in the open-loop mode. Light source is a continuous-wave laser ($\lambda = 1058$ nm).

The intensity for the two beams interfering in PSI is given as [7]:

$$I_n(x,y) = A(x,y) + B(x,y)\cos\left(\phi(x,y) + \theta_n\right), \tag{1}$$

where $I_n(x,y)$ is the intensity at the image pixel (x,y), $A(x,y)$ is the background intensity, $B(x,y)$ is the fringe or intensity

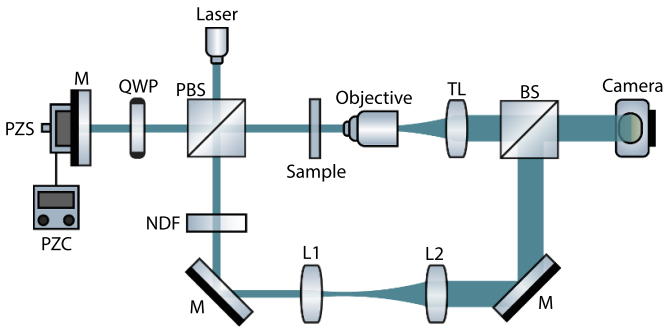

Figure 1. Phase microscopy setup. BS: Beam splitter. PBS: Polarized BS. NDF: Neutral density filter. QWP: Quarter waveplate. TL: Tube lens. M: Mirror. PZS, PZC: Piezo stage and controller. L1, L2: Lenses for enlarging reference beam. Objective: Thorlabs LMH-20X-532. Laser: continuous-wave, $\lambda = 1.058\,\mu$m.

modulation, and $\phi(x,y)$ and θ_n are the wavefront phase and a given phase shift, respectively. The subscript n denotes the interferogram frame index. For linear phase shifts, i.e. $\theta_n = n\Delta\theta$, it is clear from equation (1) that, intensity at each pixel varies sinusoidally as a function of the introduced phase shift:

$$I_n(x,y) = A(x,y) + B(x,y)\cos\left(\phi(x,y) + n\Delta\theta\right). \tag{2}$$

The nonshifted phase of this function corresponds to the wavefront phase $\phi(x,y)$ and it can be retrieved using temporal Fourier analysis with respect to the shifted phase. FT of the intensity with respect to the n (temporal) dimension can be expressed in terms of the frequency of the phase-shifting (ω) as:

$$\tilde{I}_\omega(x,y) = FT_n[I_n(x,y)]. \tag{3}$$

Subscript n indicates that Fourier transform is in the frame index dimension. For frequency $\omega_{\max}$ corresponding to the most dominant component in the Fourier spectrum, the complex amplitude can be written as:

$$\tilde{I}_{\omega_{\max}}(x,y) = \sum_{n=1}^{N} I_n(x,y)e^{-in\omega_{\max}}, \tag{4}$$

where N is the total number of interferograms. The phase of the interferogram $\phi(x,y)$ is stored in the Fourier domain as:

$$\tilde{I}_{\omega_{\max}}(x,y) = |\tilde{I}_{\omega_{\max}}(x,y)|e^{i\phi(x,y)}. \tag{5}$$

The wavefront phase then can be easily determined by:

$$\phi(x,y) = \arg\left[\tilde{I}_{\omega_{\max}}(x,y)\right]. \tag{6}$$

Correct determination of $\omega_{\max}$, as well as recording the data in multiples of the period is required for accurate phase extraction. This in turn requires precise control on θ_n. Equation (1) may deviate from a sinusoidal waveform as a result of phase shift errors (or intended random phase-shifting), back-reflections, nonlinearities in detectors, all presenting challenges in retrieving the wavefront phase. Wavefront reconstruction from nonsinusoidal and even nonperiodic intensity

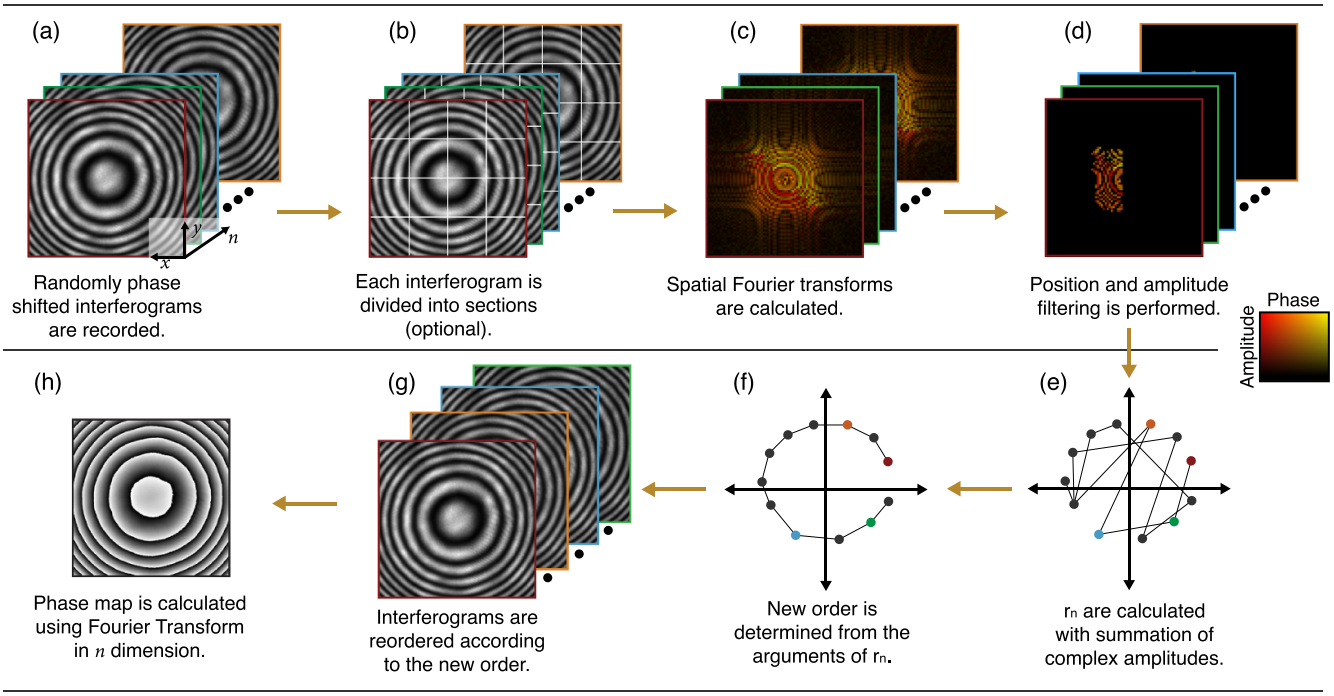

Figure 2. The methodology is explained through a series of steps. Recorded interferograms are shown in (a), with borders colored according to the interferogram order (first image shown with red). The optional sectioning procedure is shown in (b). The spatial FT of each interferogram is shown in (c). Position and amplitude filtering on the Fourier spectra is given in (d), with a representative case illustrated in the red-framed image. The complex maps in (c) and (d) are color-coded where hue is associated with the phase, and brightness is associated with the amplitude. The color map is shown at the right side of the figure. Calculated r_n are shown in (e), reordered r_n are shown in (f), reordered interferograms are shown in (g) and finally, the phase map calculated with FT in n dimension is shown in (h). If the image is divided into sections as demonstrated in (b), the steps from (c) to (h) are implemented for each section. Then, phase maps from the individual sections are stitched together to form the complete phase map.

waveforms stands at the forefront of this work. We present a spatial FT-based method that, to the best of our knowledge, for the first time allows one to reorganize arbitrary and randomly phase-shifted interferograms in the order of increasing phase shift (figure 2), so that the intensity at each pixel varies as a sinusoidal function of the phase shift. Interference pattern with random phase shifts (θ_n) can be described with Euler's identity as:

$$I_n(x,y) = A(x,y) + \frac{B(x,y)}{2} e^{i\phi(x,y)} e^{i\theta_n} + \frac{B(x,y)}{2} e^{-i\phi(x,y)} e^{-i\theta_n}. \tag{7}$$

We evaluate the two-dimensional spatial FT of the intensity:

$$U_n(\nu_x,\nu_y) = \mathrm{FT}_{x,y}[I_n(x,y)], \tag{8}$$

where ν_x, ν_y are the spatial frequencies in x and y directions, respectively. Then combining equations (7) and (8) yields:

$$U_n(\nu_x,\nu_y) = \mathrm{FT}_{x,y}[A(x,y)] + \mathrm{FT}_{x,y}\left[\frac{B(x,y)}{2} e^{i\phi(x,y)}\right] e^{i\theta_n} + \mathrm{FT}_{x,y}\left[\frac{B(x,y)}{2} e^{-i\phi(x,y)}\right] e^{-i\theta_n}. \tag{9}$$

The three terms can be written compactly as:

$$U_n(\nu_x,\nu_y) = A + B^+ e^{i\theta_n} + B^- e^{-i\theta_n}. \tag{10}$$

$U_n(\nu_x,\nu_y)$ is obtained from $I_n(x,y)$, therefore, it identifies the nth interferogram. A, B^+, and B^- are complex quantities and A does not depend on θ_n. For increasing θ_n, $B^+e^{i\theta_n}$ and $B^-e^{-i\theta_n}$ are phasors with increasing and decreasing phase, respectively. Due to these two components, $U_n(\nu_x,\nu_y)$ generates an ellipse in the complex domain. If we consider a single interferogram in this set (denoted as m), selected among the set of interferograms (denoted as n), the mth element of the ellipse refers to the mth interferogram and the position on the ellipse is determined by θ_m. Thus, even in the case that θ_n is random, the order of θ_m relative to other indices can be inferred by the relative position of $U_m(\nu_x,\nu_y)$ on the ellipse. So, the frames can be reordered such that θ_n is monotonically increasing. We exploit this approach of reordering to remove the randomness in the phase shifts.

$U_n(\nu_x,\nu_y)$ is an array of spatial frequencies, where each coordinate (ν_x,ν_y) generates an ellipse. To identify each interferogram with a single quantity, instead of an array, a selection and summation procedure is performed. We start by selecting spatial frequencies with comparatively high values of $\sum_n |U_n(\nu_x,\nu_y)|$. The pixel with indices (ν_x,ν_y) is selected if:

$$\sum_{n=1}^{N} |U_n(\nu_x,\nu_y)| > \mathrm{Percentile}\left(\sum_{n=1}^{N} |U_n(\nu_x,\nu_y)|, p\right). \tag{11}$$

Here, the function Percentile(S,p) returns the value corresponding to the highest pth percentile in the set S. We determined in our experiments and simulations that $p=2$ yields consistent and accurate results. The choice of p is amenable to further optimization.

Then, the ellipse generated by $U_n(\nu_x,\nu_y)$ oscillates either in the order of increasing or decreasing θ_n, depending on which of the phasor magnitudes ($|B^+|$ or $|B^-|$) is larger. The summation of ellipses with opposing oscillation directions intensifies the ellipse's flattening, thereby hindering the order evaluation. The oscillation directions of $U_n(\nu_x,\nu_y)$ and $U_n(-\nu_x,-\nu_y)$ are inherently opposite. It is imperative to select one side of the spectrum to ensure coherent ellipse oscillation, filtering out the opposing side. We achieved this through filtering in the Fourier domain, as implemented in our approach:

$$U_n(\nu_x,\nu_y>0)=0. \tag{12}$$

Since interferograms are real-valued maps, filtering out half of the spectrum results in no information loss. The amplitude- and position-based filtering is illustrated in figure 2(d). After the selection of the spatial frequencies (ν_x,ν_y), $U_n(\nu_x,\nu_y)$ are summed to arrive at the operational parameter r_n:

$$r_n=\sum_{\nu_x}\sum_{\nu_y}U_n(\nu_x,\nu_y)=\alpha+\beta^+e^{i\theta_n}+\beta^-e^{i\theta_n}, \tag{13}$$

where α, β^+, and β^- are complex quantities corresponding to:

$$\begin{aligned}\alpha&=\sum_{\nu_x}\sum_{\nu_y}\mathrm{FT}_{x,y}[A(x,y)],\\ \beta^+&=\sum_{\nu_x}\sum_{\nu_y}\mathrm{FT}_{x,y}\left[\frac{B(x,y)}{2}e^{i\phi(x,y)}\right],\\ \beta^-&=\sum_{\nu_x}\sum_{\nu_y}\mathrm{FT}_{x,y}\left[\frac{B(x,y)}{2}e^{-i\phi(x,y)}\right].\end{aligned} \tag{14}$$

3. Experimental results

In what follows, we detail the application of the method to a set of randomly phase-shifted interferograms obtained in a phase microscopy setup (figure 1). The real versus imaginary part of r_n for the as-recorded sequence is plotted in figure 3(a). Then, by considering the argument of r_n the data is reordered, and plotted in figure 3(b). The corresponding plots of intensity versus frame index n are shown for as-recorded and reordered sequences in figures 3(c) and (d), respectively. The red cross and cyan square data points show the first two interferograms in the sequences. While the intensity of the as-recorded data is not a periodic function (figure 3(c)), the sinusoidal pattern of the intensity is recovered once the interferograms are ordered (figure 3(d)). Next, the FT of the intensity presented in figure 3(d) is evaluated to retrieve the object phase $(\phi(x,y))$ by using equations (4)–(6), while this is not possible for the as-recorded data presented in figure 3(c). This ability

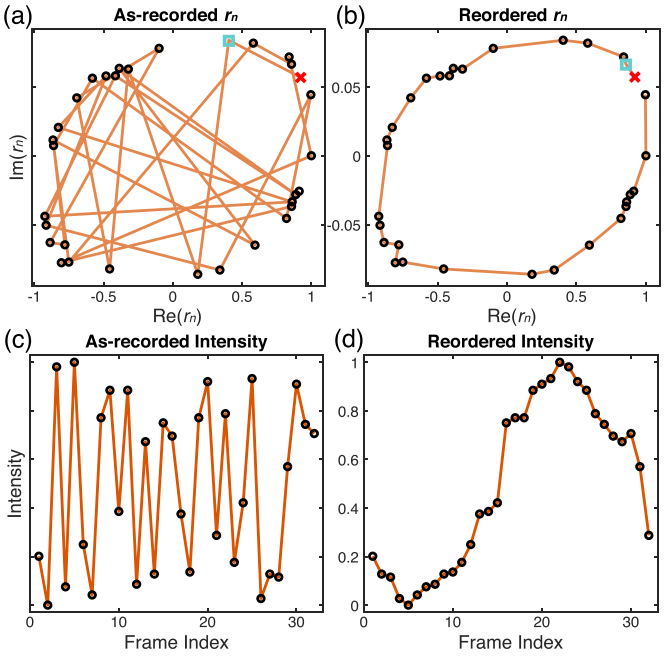

Figure 3. Implementation of the method to 32 randomly phase-shifted interferograms. The real vs. imaginary parts of r_n are plotted for the (a) as-recorded and (b) reordered data. r_n is translated to the origin by subtracting the mean. In (b), the data are plotted in the order of increasing arg(r_n). The red cross and cyan square data points represent the 1st and 2nd interferograms, respectively. Frame index vs. intensity is plotted for a single pixel for (c) as-recorded and (d) reordered data. The sinusoidal form of the intensity has been recovered in (d), when the ordered frame indices obtained in (b) are used for plotting.

to recover the order from randomly phase-shifted frames may have significance in a wide range of phase retrieval applications.

For performance evaluation, we present an error analysis. We first extract the phase map of a bare silicon wafer $(\phi_{\mathrm{ref}}(x,y))$ using the proposed method with a high number of interferograms (128 frames) with constant phase steps ($\theta_n=n\Delta\theta$). Employing such a large number of frames with constant phase steps minimizes experimental errors including phase shift inaccuracy and nonuniform phase shifting due to the averaging effect [5, 23]. The resulting phase map is used as the reference for further error quantification, which is a typical approach followed for obtaining a reference phase map [15].

We then recorded randomly phase-shifted data with 32 frames (figure 4(a)) to extract the phase map $(\phi_{\mathrm{rand}}(x,y))$ as shown in figure 4(b). The phase error is calculated as $\delta\phi(x,y)=\phi_{\mathrm{rand}}(x,y)-\phi_{\mathrm{ref}}(x,y)$, given in figure 4(c). For both $\phi_{\mathrm{rand}}(x,y)$ and $\phi_{\mathrm{ref}}(x,y)$, first the interferograms are sorted, then the phase is acquired with temporal FT using equations (4)–(6). High frequency components that lie beyond the resolution limit of the microscope ($\lambda/(2\mathrm{NA})\sim1.3\,\mu$m) are low-pass filtered. This analysis has been repeated for 10 different randomly phase-shifted data sets. The results reveal that, on average, the method can retrieve the phase map

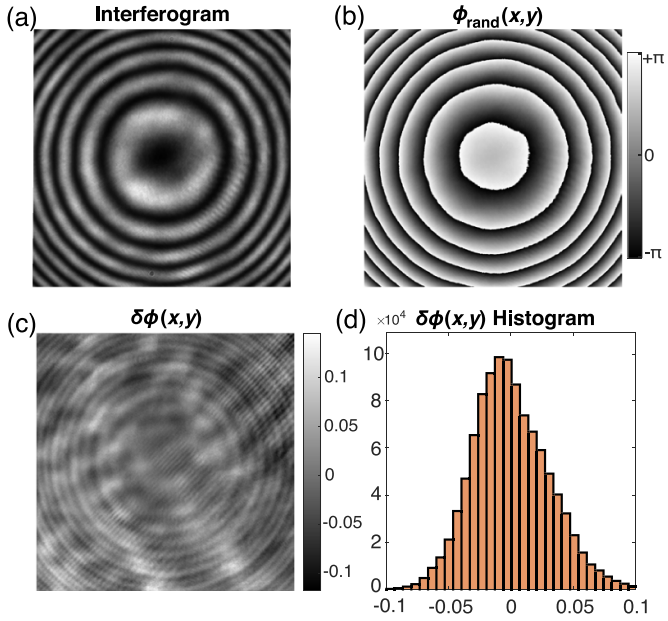

Figure 4. Phase imaging of a bare silicon wafer. (a) One of the 32 randomly phase-shifted interferograms. (b) Phase map extracted using the method. (c) Calculated phase error. (d) Histogram of $\delta\phi(x,y)$, resulting in 0.060 rad RMS error.

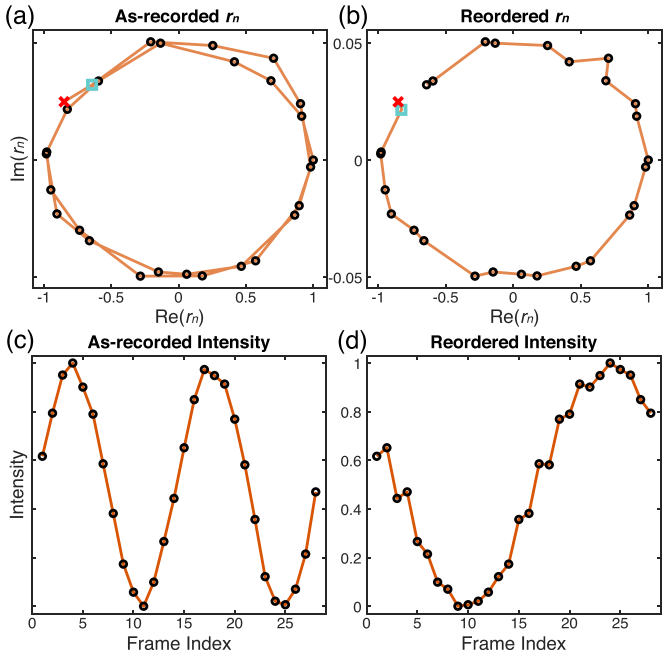

Figure 5. Implementation of the method with 28 uniformly phase-shifted interferograms. (a) The real vs. imaginary parts of r_n are plotted for the (a) as-recorded and (b) reordered data. In (b), the data are reordered based on $\arg(r_n)$. The red cross and cyan square data points represent the 1st and 2nd interferograms, respectively. The frame number vs. intensity for a single pixel is plotted using the (c) as-recorded and (d) reordered data.

with a standard deviation (RMS error) of $\sigma(\delta\phi(x,y)) = 0.060$ rad, as seen in the histogram in figure 4(d). Considering the wavelength, this corresponds to a resolution of around 10 nm. It is evident from these findings that the proposed method enables accurate PSI measurements using randomly phase-shifted interferograms. Consequently, it eliminates the need for high-accuracy and expensive phase-shifting equipment. The results also demonstrates a direct indication of robustness of the method to parasitic phase shifts due to environmental instability.

Another aim of the method is to improve the phase extraction from uniformly phase-shifted data. This is evaluated by extracting the phase from 28 uniformly phase-shifted interferograms in two different ways. In the first case, temporal FT was directly applied for calculating the phase, without reordering the data. In the second case, the data was first reordered and then the temporal FT was applied to extract the phase. In both cases, phase is acquired with FT using equations (4)–(6). For the second case, the r_n value for the as-recorded and reordered data can be seen in figures 5(a) and (b), respectively, along with corresponding intensity plots for a pixel shown in figures 5(c) and (d). Phase maps extracted with and without reordering were compared with the reference phase map to compute the error, as described earlier. Both analyses were repeated for 10 different data sets. Results show that the RMS error is reduced from 0.032 rad to 0.027 rad by reordering the data, yielding $\sim$17% improvement. This is because when the data is not reordered, phase shift between the interferograms is not evaluated and positions of the frames are accepted as they are. However, when the data is reordered, the phase shift of each interferogram is evaluated with respect to the other frames and thus the phase shift errors can be reduced. As a result, the method is shown to be advantageous even in the case of a high-accuracy piezoelectric stage, corroborating its power as a fast, accurate, and easy measurement approach. As expected, uniformly phase-shifted interferograms result in less error than randomly phase-shifted interferograms (0.027 rad vs. 0.060 rad). A comparison of figures 3(d) and 5(d) shows that the sinusoidal obtained from uniform phase shifting is more uniform, thus the phase can be extracted more accurately with temporal FT.

4. Simulation methodology

Finally, we evaluate the robustness of our method to commonly investigated error sources, including random intensity noise, intensity harmonics, nonlinear phase shifts, and compare our results with those of a recent work based on GIA [15]. In [15], GIA was compared with five other work and shown to achieve the best result in terms of error. So we have implemented the simulation scheme adapted in [15] to incorporate the same type and magnitude of errors, and used our method to extract the phase. The procedure for interferogram creation as detailed in [15] is concisely recapitulated below. The model for the interferogram, specific to Simulation Set X as presented in [15], is described as follows:

$$I_n(x,y) = A(x,y) + \mathrm{AGWN}_n(x,y) + \sum_{k=1}^{P} B_k(x,y)\cos\left(k\phi(x,y) + k\theta_n(x,y)\right). \quad (15)$$

The function $\mathrm{AGWN}_n(x,y)$ denotes the additive Gaussian white noise, with standard deviation 0.4, mean 0, and is randomly generated for each frame. Simulation set incorporates intensity harmonics, represented with the summation $(\sum_{k=1}^{P}())$ term, which is calculated based on the 'gamma model' [24], with $\gamma = 1.5$. Background intensity $(A(x,y))$ is modeled as:

$$A(x,y) = \frac{1}{2} - \frac{1}{4}\left[\frac{(x - N_x/2)^2 + (y - N_y/2)^2}{(N_x/2)^2 + (N_y/2)^2}\right], \quad (16)$$

where $N_x = N_y = 1024$, denoting the pixel number in x and y axes. The ground truth phase map $(\phi(x,y))$ is modeled as:

$$\phi(x,y) = 10 \times \mathrm{peaks_s}(x,y) + \frac{1}{4} \times y, \quad (17)$$

where $\mathrm{peaks_s}()$ is the 'peaks' function of MATLAB, scaled in the range $[0,2\pi]$. Then, spatially nonuniform phase shifts $(\theta_n(x,y))$ are formulated in terms of Maclaurin polynomials as:

$$\theta_n(x,y) = \sum_{u=0}^{Q}\sum_{v=0}^{u} \frac{\alpha_{uv,n} x^u y^{u-v}}{(N_x - 1)^u (N_y - 1)^{u-v}}, \quad (18)$$

where $\alpha_{uv,n}$ are coefficients of the Maclaurin polynomials, chosen randomly with mean 0 and standard deviation 0.5, except for $\alpha_{00,n}$, which is taken as: $\alpha_{00,n} = n\pi/4$.

One of the simulated interferogram frames along with the phase map extracted by our method are shown in figures 6(a) and (b), respectively. Figure 6(c) shows the error calculated as a function of the number of frames N used for extracting the phase. The figure plots the error for two different cases with and without sectioning, which is explained below.

The robustness of the method to nonuniform phase-shift distribution $(\theta_n(x,y))$ can be further improved by a minor modification to the method, which we call sectioning (figure 2(b)). Sectioning reduces the error substantially for each N, as shown in figure 6(c). With this approach, instead of operating the algorithm on the entire frame at once, the algorithm is applied to smaller subsections of the frames so that $\theta_n(x,y) \approx$ constant. The complete phase map is obtained by stitching of phase maps of the subsections. For r_n to create accurate ellipses, each subsection should enclose a full fringe, so the number of subsections is determined by the maximum fringe size. 24×24 subsections have been used in the simulations.

5. Simulation results

Simulated patterns are processed with our method to extract the phase maps, and then the error is calculated by evaluating the difference between these phase maps and the true phase map. Our results compared to those of other six methods reported in the literature are shown in table 1. Our method (FT-only) results in less error (0.066 vs. 0.068–0.184) than the other methods with $N = 48$ interferograms. Although the other methods use $N = 8$ interferograms, the increased number of frames in our case does not produce a disadvantage since the entire phase extraction procedure, including the data acquisition of $N = 48$ interferograms, takes only ∼93 s with our method. The GIA algorithm [15] produces the closest error to ours, but it requires a larger computational time (∼559 s). Considering that it would take 14.93 s to acquire 8 frames with our setup, their total phase extraction time is estimated as 573.74 s. These results demonstrate that our method is 6 times faster (574 s / 93 s) for a similar level of error (0.066 rad vs. 0.068 rad). Notably, we can further reduce the error to 0.058 rad by increasing N to 64, with a total phase extraction time of only 125 s. The data acquisition times plotted in figure 6(d) are recorded by automatizing the stage and the camera. A standard office computer is used for the computations (CPU: 11th Gen. Intel i5-11 500 @ 2.70 GHz, 12 cores, RAM: 32 GB).

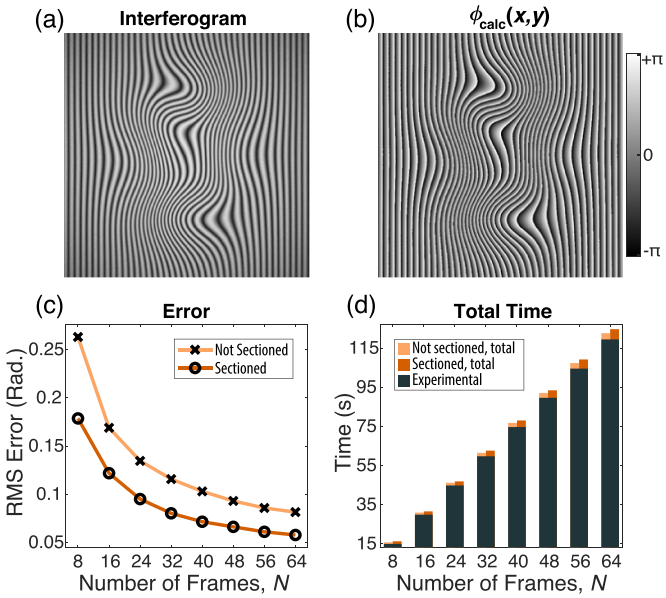

Figure 6. (a) An example interferogram generated for the simulations. (b) Phase map extracted using the method. (c) Phase error computed as a function of frame number with and without sectioning. Each data point corresponds to an average of 100 simulation sets. (d) Data acquisition time (black bars); combined computational and data acquisition time with sectioning (orange bars) and without sectioning (yellow bars).

6. Discussion

The findings presented in this report constitute a Fourier-transform-only approach for interferometry. The developed method accurately extracts phase information from randomly phase-shifted interferograms, with a notably low experimental error of 0.060 radians. Moreover, the accuracy in scenarios involving high-precision stages is further increased by 17%

Table 1. Performance comparison for simulation with six other methods in the literature. Our method is labeled as FT-only, where results for $N = 8, 48, 64$ are shown, for other methods $N = 8$. Our method is the fastest, and has the least error for $N \geqslant 48$. Higher number of frames in our method is justified with lower total time compared to other low error methods tabulated (GIA, MPSI, PTI). Our experimental time is reported to indicate typical experimental times. [Reprinted] with permission from [15] © The Optical Society.

Method		FT-only		GIA [15]	MPSI [25]	PTI [26]	Xu's [27]	AIA [11]	Hoang's [28]
Error (Rad)	0.179	0.066	0.058	0.068	0.094	0.095	0.173	0.183	0.184
N (Frame Number)	8	48	64	8	8	8	8	8	8
Experimental Time (s)	14.93	89.59	119.56	-	-	-	-	-	-
Computational Time (s)	1.33	3.84	5.24	558.84	186.69	882.67	59.33	7.73	145 024.84

(0.032 rad to 0.027 rad), which highlights its suitability for high-end applications.

One of the salient features of the method is its superior performance in the presence of various error sources, such as higher harmonics, intensity noise, and nonuniform phase shifting, both in terms of error reduction and computational efficiency. In the Supplementary Material, we provide further evidence of our method's robustness through simulations involving a speckle noise model detailed in [29] and random fringe patterns. These simulations confirm that our approach performs well in the presence of speckle noise and effectively navigates the complexities of intricate fringe patterns. An essential advantage of this approach lies in its simplicity, leveraging the well-established Fourier theory, which is not only computationally efficient but also highly accessible to researchers, without the need for expensive equipment and complex algorithms.

In parallel, some of the limitations of the approach arise from reliance on this mathematical tool. First, since the construction of accurate ellipses is contingent upon spatial Fourier transforms, it is necessary for each frame to include at least a single fringe. However, this is consistent with numerous optical and signal processing systems, ensuring adequate data sampling. Further, the reliance on FT in the n dimension implies that despite its capacity to accommodate random phase shifts, it exhibits optimal performance with regular phase shifting. Finally, achieving high-precision phase maps may demand a relatively larger number of frames. However, this seemingly increased data acquisition requirement is outweighed by the significant reduction in overall phase extraction time compared to alternative methods, as evidenced in section 5.

7. Conclusion

In this work, we demonstrate a Fourier-transform-based phase imaging method that can extract the phase from unknown randomly phase-shifted interferograms with high precision (experimentally with an error of 0.060 rad). Further, the method is shown to improve the phase error by 17% even in the case of a high-accuracy piezoelectric stage. As demonstrated through simulations including higher harmonics, intensity noise, and nonlinear phase shifting; the method extracts the phase with lower error, in less time (combined experimental and computational time) with reduced complexity compared to the state-of-the-art. Thus, the method is capable of combining high measurement precision with high speed, noise resilience, simplicity, and reduced computational effort characteristics of the well-established Fourier theory. This advance fulfills the need for precise phase extraction under general error sources, including environmental errors such as vibrations, air flow or temperature fluctuations, and removes restrictions on expensive equipment or advanced algorithms.

Data availability statement

The data cannot be made publicly available upon publication because they are not available in a format that is sufficiently accessible or reusable by other researchers. The data that support the findings of this study are available upon reasonable request from the authors.

Funding

The authors acknowledge support from the Turkish Academy of Sciences (TÜBA-GEBİP Award), and the TÜBİTAK-1001 project (Grant No. 121F387).

Conflicts of interest

The authors declare that there are no conflicts of interest.

ORCID iDs

Alperen Saltik https://orcid.org/0009-0008-5654-3713
Sueda Saylan https://orcid.org/0000-0002-1994-0110
Onur Tokel https://orcid.org/0000-0003-1586-4349

References

[1] Creath K 1988 *V Phase-Measurement Interferometry Techniques* (Elsevier) pp 349–93
[2] Bruning J H, Herriott D R, Gallagher J E, Rosenfeld D P, White A D and Brangaccio D J 1974 Digital wavefront measuring interferometer for testing optical surfaces and lenses *Appl. Opt.* **13** 2693–703
[3] Wyant J C, Koliopoulos C L, Bhushan B and George O E 1984 An optical profilometer for surface characterization of magnetic media *ASLE Trans.* **27** 101

[4] Hariharan P, Oreb B F and Eiju T 1987 Digital phase-shifting interferometry: a simple error-compensating phase calculation algorithm *Appl. Opt.* **26** 2504
[5] Schwider J, Burow R, Elssner K-E, Grzanna J, Spolaczyk R and Merkel K 1983 Digital wave-front measuring interferometry: some systematic error sources *Appl. Opt.* **22** 3421
[6] Surrel Y 1996 Design of algorithms for phase measurements by the use of phase stepping *Appl. Opt.* **35** 51
[7] Schreiber H and Bruning J H 2007 *Phase Shifting Interferometry* (Wiley) pp 547–666
[8] Surrel Y 1993 Phase stepping: a new self-calibrating algorithm *Appl. Opt.* **32** 3598
[9] Greivenkamp J E 1984 Generalized data reduction for heterodyne interferometry *Opt. Eng., Bellingham* **23** 234350
[10] Zhu H and Guo H 2022 Anti-aliasing phase reconstruction via a non-uniform phase-shifting technique *Opt. Express* **30** 3835
[11] Wang Z and Han B 2004 Advanced iterative algorithm for phase extraction of randomly phase-shifted interferograms *Opt. Lett.* **29** 1671
[12] Vargas J, Quiroga J A and Belenguer T 2011 Phase-shifting interferometry based on principal component analysis *Opt. Lett.* **36** 1326
[13] Escobar M A, Estrada J C and Vargas J 2020 Phase-shifting vu factorization for interferometry *Opt. Lasers Eng.* **124** 105797
[14] Gomez-Conde J C and Meneses-Fabian C 2020 Real-time phase step measurement using the volume enclosed by a surface algorithm in self-calibrating phase-shifting interferometry *Measurement* **153** 107412
[15] Chen Y and Kemao Q 2021 General iterative algorithm for phase-extraction from fringe patterns with random phase-shifts, intensity harmonics and non-uniform phase-shift distribution *Opt. Express* **29** 30905
[16] Larkin K G and Oreb B F 1992 Design and assessment of symmetrical phase-shifting algorithms *J. Opt. Soc. Am.* A **9** 1740
[17] Freischlad K and Koliopoulos C L 1990 Fourier description of digital phase-measuring interferometry *J. Opt. Soc. Am.* A **7** 542
[18] Yang Z, Albrow-Owen T, Cai W and Hasan T 2021 Miniaturization of optical spectrometers *Science* **371** eabe0722
[19] Guo H and Zhang Z 2013 Phase shift estimation from variances of fringe pattern differences *Appl. Opt.* **52** 6572
[20] Leach R 2011 *Optical Measurement of Surface Topography* vol 8 (Springer)
[21] Nolte D D 2011 *Optical Interferometry for Biology and Medicine* vol 1 (Springer)
[22] Kulkarni R and Rastogi P 2016 Optical measurement techniques-a push for digitization *Opt. Lasers Eng.* **87** 1
[23] Hao Q, Zhu Q and Hu Y 2009 Random phase-shifting interferometry without accurately controlling or calibrating the phase shifts *Opt. Lett.* **34** 1288
[24] Liu K, Wang Y, Lau D L, Hao Q and Hassebrook L G 2010 Gamma model and its analysis for phase measuring profilometry *J. Opt. Soc. Am.* A **27** 553
[25] Deck L L 2014 Model-based phase shifting interferometry *Appl. Opt.* **53** 4628
[26] Duan M, Zong Y, Zhu R and Li J 2021 Phase-tilt iteration: accurate and robust phase extraction from random tilt-shift interferograms *Opt. Lasers Eng.* **142** 106595
[27] Xu J, Xu Q and Chai L 2008 An iterative algorithm for interferograms with random phase shifts and high-order harmonics *J. Opt. A: Pure Appl. Opt.* **10** 095004
[28] Hoang T M, Wang Z, Vo M, Ma J, Luu L and Pan B 2011 Phase extraction from optical interferograms in presence of intensity nonlinearity and arbitrary phase shifts *Appl. Phys. Lett.* **99** 031104
[29] Servin M, Estrada J, Quiroga J, Mosiño J and Cywiak M 2009 Noise in phase shifting interferometry *Opt. Express* **17** 8789